Machine Learning-assisted Single Vessel Analysis of Nanoparticle Permeability in Tumour Vasculatures

Xinglu Huang (huangxinglu@nankai.edu.cn)
Nankai University
Mingsheng Zhu
Nankai University
Jie Zhuang
Nankai University
Zhe Li
University of Science and Technology of China
Qiqi Liu
Nankai University
Zhanxia Gao
Nankai University
Adam Midgley
Nankai University https://orcid.org/0000-0002-7622-0275
Tianyi Qi
Nankai University
Rongping Zhao
Nankai University
Zhixuan Zhang
Nankai University
Deling Kong
Nankai University https://orcid.org/0000-0002-2961-9267
Jie Tian
CAS Key Laboratory of Molecular Imaging, Institute of Automation, Chinese Academy of Sciences
https://orcid.org/0000-0003-0498-0432
Xiyun Yan
Institute of Biophysics, Chinese Academy of Sciences https://orcid.org/0000-0002-7290-352X

Article

Keywords:

Posted Date: July 12th, 2022

DOI: https://doi.org/10.21203/rs.3.rs-1829585/v1

Version of Record: A version of this preprint was published at Nature Nanotechnology on February 13th, 2023. See the published version at https://doi.org/10.1038/s41565-023-01323-4.

Abstract

The central dogma of nanoparticle delivery to tumours through enhanced leakiness of vasculatures has become a topic of debate in recent years. To address this problem, we created a single-vessel quantitative analysis method by taking advantage of protein-based nanoprobes and image segmentation-based machine learning technology (Nano-ISML). Using Nano-ISML, we quantified > 50,000 individual blood vessels from 32 tumour models, which revealed highly heterogenous vascular permeability of protein-based nanoparticles in different tumours and blood vessels. There was > 20-fold difference in the percentage of high-permeable vessels in different tumours and > 100-fold penetration ability in vessels with the highest permeability compared to vessels with the lowest permeability. We demonstrated that this phenomenon resulted from diversified vascular penetration mechanisms. Specifically, passive extravasation and trans-endothelial transport were dominant mechanisms for high-permeable and low-permeable tumour vessels, respectively. Furthermore, to exemplify Nano-ISML assisted rational design of desirable nanomedicines, we developed genetically tailored protein nanoparticles that improved trans-endothelial transport in low-permeable tumours. Our study delineates the heterogeneity of tumour vascular permeability and defines a direction for rational design of the next generation anti-cancer nanomedicines.

Introduction

Delivery of intravenously administered therapeutics to solid tumours faces multiple barriers[1–3]. Blood vessels are the first barrier beyond systemic circulation. Transport across endothelial cells is an essential process for boosting the delivery efficiency of anti-cancer agents[4,5]. In tumour blood vessels, the gaps between endothelial cells (e.g., inter-endothelial gaps) and transcellular fenestrae (e.g. vesiculo-vacuolar organelle; VVO) within the walls of tumour blood vessels allow oxygen and nutrients to directly cross the endothelium[6–8]. On the basis of this tumour blood vessel leakiness, the enhanced penetration and retention (EPR) was first observed in 1986[9]. The EPR effect is a mechanism that involves the increased passive extravasation of blood vessels and the progressive accumulation of macromolecules into solid tumour tissues, and it has been considered a critical rationale for the development of tumour-targeting nanoscale carriers. However, only approximately ten nanomedicines have been approved for clinical use in tumour therapy over the past three decades[10]. The limited clinical translation of nanomedicines has pushed researchers to deliberate the extent of mechanisms involved in nanoparticle-based delivery into tumour tissues. In a recent investigation, up to 97% of nanoparticles were demonstrated to enter tumours through an active trans-endothelial transport mechanism as opposed to the mechanism of passive extravasation[11]. This conclusion was controversial in the community, but did provide a ‘wake-up call’ to shift research towards delineating the heterogeneity of vascular permeable mechanisms. However, the current lack of available quantitative strategies has hampered progress in understanding vascular permeability of nanoparticles.

The quantitative analysis of individual blood vessels represents an accomplishment capable of addressing the extent of tumour vascular permeability, but is a time-consuming, laborious, and resource-intensive task. Following deep learning of the trained data, the machine learning (ML) can be employed to timely analyse big data, and identify trends and patterns not obvious to human operators[12–16]. Inspired by the advantages presented by ML, we sought to fill the knowledge gap in high-throughput quantification of vascular permeability by originating a single-vessel analysis approach on the basis of protein-based nanoprobes and image segmentation-based ML technology (Nano-ISML). Using Nano-ISML, we aimed to answer three key questions on nanoparticle delivery to tumours: (i) is there heterogeneous vascular permeability in different tumours and blood vessels, and if so, how to quantifiably classify differential tumour permeability; (ii) what is the potential mechanism of permeability in different vessels, and (iii) whether the approach facilitates modulating the changes in vascular permeability, thereby guiding the development of personalized delivery strategies. By answering these questions, we will contribute valuable evidence to calm down about the controversy of vascular permeability. Additionally, the Nano-ISML strategy we established will facilitate the wider adoption of quantitative methodology and monitoring the efficiency of nanoparticle delivery to tumour tissues.

Results

To perform quantitative analysis of vascular permeability, at least two aspects are prerequisite: (i) a suitable probe capable of indicating vascular translocation from lumen to extravascular space; and (ii) a quantitative analysis tool with the capacity to perform high-throughput analysis of thousands of individual blood vessels. We thus originated a single-vessel analysis approach by combining vascular permeability of fluorescent dye-labelled protein nanoprobes with the advantages gained from ML in image segmentation. The workflow is shown in Fig. 1a. Genetically recombinant human ferritin nanocages (FTn) were chosen as model nanoparticles because they possess reproducible and homogenous size (i.e. 12 nm) and structure[17,18], and can be visualized after dye-labelling (**Supplementary Fig. 1a**). To understand the *in vivo* dynamic behaviours of FTn, we first administrated Cy5.5-labelled FTn into tumour-bearing mice for *in vivo* imaging. A burst accumulation of FTn was observed in tumours (indicated by dashed line circles), and reached a maximum accumulation at 30 minutes post-administration (**Supplementary Fig. 1b and c**). To quantitatively analyse vascular permeability of the images obtained from tumour tissue, we next developed a ML-based workflow (Fig. 1b). The first step was to pre-process the images by normalisation and gaussian smoothing of fluorescent signals. Next, the images containing vessels and FTn penetration were manually annotated, respectively. The annotated images were randomly divided into an 80% training dataset and a 20% validating dataset, followed by training with U-net convolutional neural network[19]. The third step was machine automatic segmentation and feature extraction processing, using the established models. The boundaries of blood vessel profiles and FTn coverage areas were automatically segmented from the input images, followed by the extraction of parameters derived from vessel and FTn penetration. We provided example images, including the original microscopy image (confocal), manual segmentation image (annotation), and machine segmentation image (prediction) (**Supplementary Fig. 2a**). Following the above workflow, herein termed

Nano-ISML, the models were trained using the input images randomly extracted from different tumour model types. The established two models (i.e., vessel and FTn penetration) showed ~ 90% and ~ 80% accuracy in blood vessel and FTn penetration across 32 tumour models, respectively (**Supplementary Fig. 2b**), which demonstrated the trained models were suitable for further use.

Next, we sought to evaluate the permeability of individual vessels in various tumour model types using the Nano-ISML. The images collected from various tumour types were obtained 30 minutes after administration of Cy5-labelled FTn (**Supplementary Fig. 3a**). Based on automatic machine segmentation of the images, we extracted the total FTn coverage area for each vessel (A_{red}), the coverage area of each vessel (A_{green}), the total Cy5 fluorescence intensity for each vessel (F_{red}), and the Cy5 fluorescence intensity in each vessel lumen (I_{red}) (**Supplementary Fig. 3b**). According to the above four features, we defined a series of indices for single-vessel quantitative analysis to include three aspects: blood vessels, FTn penetration, and the correlation between vessels and FTn penetration (**Supplementary Table 1**). To determine the hidden features of the images, we collected and analysed sufficiently large numbers of vessels, with at least 1,000 vessels per tumour and a total of 50,275 vessels analysed in 32 tumours (**Supplementary Fig. 4**). Nine important indices were preferentially and individually analysed for each vessel assessed, such as vessel area (VA), FTn penetration area (PA), FTn penetration amount (FA), FTn penetration area ratio (PR) and vascular permeability (VP). These indices were normalised and displayed as heatmap images, and the results of vessel, FTn and vessel-FTn indices demonstrated that blood vessel permeability across different tumour model types was highly heterogeneous (Fig. 2a). The detailed quantification analysis is listed in the **Supplementary Fig. 5** and **Supplementary Table 2.** To better understand the heterogeneity in vascular permeability, the PR and VP were chosen as the indices for further data mining. We quantified the mean PR of blood vessels in various tumours using the Nano-ISML. The representative individual vessels and their corresponding FTn penetration are shown by using the length scale-dependent geometric segmentation area (Fig. 2b). For example, at a length scale of 20 μm, the blood vessels in HT29 and HepG2 tumours showed a large area of permeability, whereas poor penetration was observed in 3LL and SKBR3 tumours. Quantification analysis demonstrated that the mean PR of all vessels in 32 tumours were ranged from 1.92 to 10.27 (Fig. 2c) and the highest vessel PR was > 100-fold greater than the lowest vessel PR (**Supplementary Fig. 5c**). We thus divided tumours into two categories by scoring tumour permeability, using a cut-off PR value of 4, thereby grouping tumours in high permeable (HP)- and low permeable (LP)-tumour categories. The results indicated that Dang, Hep3B, HepG2, HT29, MCF-7, MX-1, PC3, SMMC-7721 and SW-1990 were HP-tumours, whereas other tumours showed low permeability. To further elucidate the penetration ability of individual vessels, Violin plot analyses were performed to visualize the distribution of the VP values. As shown in Fig. 2d, the highly heterogeneous distribution of VP was observed for the blood vessels of each tumour, indicating that vascular permeability was highly heterogeneous for different vessels within the same tumour type. Moreover, the distribution of the dominant vessel population was greatly varied among the different tumour model types. The major population of 3LL, 4T1, A375, B16, CT26, HT1080, MC38, MDA-MB-231, Miapaca-2, SKBR3 and U87 distributed at VP values of approximately 0.1. In contrast, Dang, Hep3B, HepG2, HT29, MCF-7, MX-1, PC3, SMMC-7721 and SW-1990 presented high permeability, as evidenced by

the major population at approximately 0.8. For BGC-823 and K180, the VP values showed broad distribution (0.1–0.8), and for MB49 and Panc02, VP values were distributed in the middle range (0.4–0.5). Following Violin plot analyses of VP distribution, we classified blood vessels of each tumour into three permeability types, according to their VP values, including LP (< 0.3)-, MP (medium permeable, 0.3–0.6)- and HP (> 0.6)-vessels. The percentage distribution of the three kinds of vessels in each tumour are displayed in Fig. 2e. The HP-vessels of HT29 account for 66.3% of all vessels but comprised only 12.3% of LP-vessels. In contrast, there were 3.3% and 6.8% HP-vessels observed in SKBR3 and 3LL, respectively. These quantification analyses revealed that the VP was dependent on tumour type and was a result of heterogeneous susceptibility to penetration exhibited by different vessels. Additionally, sequential tissue sectioning of three permeable tumours was performed, and the results revealed that the VP values of tumours was not significantly affected by different tissue layers with defined tissue section thickness (**Supplementary Fig. 6**).

To explore the penetration mechanism of tumour vessels, we used a Zombie model to assess the penetration of FTn by perfusing with a fixative to deactivate cellular activity while maintaining vessel architecture. This model allowed us to study the extent of the contribution of passive extravasation and active trans-endothelial transport[11]. Using the Nano-ISML technology established above, HT29 (i.e., HP-tumour) and 3LL (i.e., LP-tumour) tumours were chosen to analyse FTn penetration in Zombie models and control tumour-bearing mice. We found that the Violin plot distribution of VP in control HT29 tumours were consistent with Zombie HT29 tumours (Fig. 3a). However, compared to control 3LL tumours, there was a significant reduction in VP observed in Zombie 3LL tumours. Quantification analysis of the different permeable vessels demonstrated that the percentage of HP-vessels in Zombie HT29 were not substantially changed compared to the control tumours, whereas 39.1% of MP-vessels in control 3LL were decreased to 20.0% in the Zombie HT29 tumours (Fig. 3b). The results implied that the FTn penetration in HP-tumours and HP-vessels was mainly dependent on passive extravasation mechanisms, whereas active trans-endothelial transport played a leading role in LP tumours.

To further understand heterogeneous penetration mechanisms, we generated iron oxide nanoparticles (IO) into hollow cavity of FTn (FTn-IO) via a biomimetic synthesis approach[20] (**Supplementary Fig. 7a**). Transmission emission microscopy (TEM) images of tumour tissues at 30 minutes showed that the individual FTn-IO were clearly visualized in the vessel lumens, endothelial lining, and extravascular space (**Supplementary Fig. 7b**). We next evaluated how FTn-IO was transported from vascular lumen to the extravascular space. Two mechanisms were identified in this process, including passive extravasation and active trans-endothelial transport. According to our TEM observations made from 73 blood vessels, we observed two passive extravasation mechanisms that participated in the direct diffusion of FTn-IO from the lumen to extravascular space, mainly including via inter-endothelial gaps (**Supplementary Fig. 8a**) and VVO (**Supplementary Fig. 8b**). The sizes of the inter-endothelial gaps were not uniform, and reached a maximum size of > 600 nm in our tumour vessel samples. VVO are grape-like clusters of interconnected vesicles, are pathways of direct connection between vasculature lumen and extravascular space, and are often found in tumour microvasculature[21,22]. Tight junctions with small gaps (~ 10 nm)

were typically found between endothelial cell-endothelial cell junctions, but we did not observe extravasated FTn-IO in their gaps (**Supplementary Fig. 8c**), revealing that the extravasation of nanoparticles is not dependent on tight junction pathway. To determine the active transport processes involved, we first explored active capture-uptake mechanisms. Three main capture-uptake mechanisms were observed under TEM, including pinocytosis, phagocytosis, and receptor-mediated endocytosis (Fig. 3c). We found that pinocytosis was a principal capture-uptake mechanism for FTn-IO by counting FTn-IO numbers. In typical endothelial cells, pinocytosis, phagocytosis, and receptor-mediated endocytosis of FTn-IO accounted for 83.3 ± 4.6%, 15.4 ± 4.1% and 1.3 ± 0.8%, respectively (Fig. 3d). After capture by endothelial cells, the protruded “arms” of the endothelial lining connect to form vesicles that are translocated into extravascular space via exocytosis. Using TEM, we observed that the diameter of the formed vesicles was highly heterogeneous in different vessels (**Supplementary Fig. 8d and e**). The vesicles reached microscale in size for the active vessels but were < 100 nm in inactive vessels (Fig. 3e, left), which are typically formed by receptor-dependent endocytosis[23]. Quantification analysis demonstrated that the vesicles larger than 100 nm in active-vessels and inactive-vessels accounted for approximately 35% and 3%, respectively (Fig. 3e, right). The active transport processes including capture, vesicle formation, transport, and exocytosis, were clearly observable (**Supplementary Fig. 8g and h**). Based on these results, we proposed the potential heterogeneous mechanisms of nanoparticle transport across tumour blood vessels (Fig. 3f). For HP-tumours, the passive extravasation *via* inter-endothelial gap and VVO comprised the predominant penetration mechanism. In addition to a small number of high-permeability vessels, nanoparticle transport to the extravascular space by the vessels in LP-tumours was predominantly dependent on active trans-endothelial transport mechanisms following the active capture of nanoparticles, mainly by pinocytosis by active vessel endothelial cells.

Modulating the vascular permeability properties of nanoparticles offers an effective approach to facilitating the enhanced efficacy of drug delivery. Uncovering the mechanisms dictating tumour vessel permeability undoubtedly defines a direction for guided design of nanoparticles. We thus sought to explore how to improve the vascular permeability of FTn in LP-tumours. We found that FTn localized in lysosomes, and subsequently, remained trapped in lysosomes following uptake by human umbilical vein endothelial cells (HUVECs) (**Supplementary Fig. 9**). Lysosomes are important organelles for inducing intracellular degradation of exogenous particles[24,25]. Thus, we hypothesized that reducing lysosome trapping to improve transport efficacy of endothelial cells would be an efficient strategy for boosting vascular permeability of FTn. Following this line of thought, we developed three FTn variants based on genetic engineering strategies. These included $(H_2E)_9$-fused FTn (H_2E-FTn), human serum albumin (HSA) bound FTn (HSA-FTn) and HSA bound H_2E-FTn (HSA/H_2E-FTn). The endosomolytic $(H_2E)_n$ peptide is capable of proton buffering to aid endosomolysis[26] and HSA is preferentially trafficked to the Golgi apparatus[27–29] followed by secretion of exocytic-vesicles and exocytosis. Specifically, H_2E-FTn was obtained by genetically inserted $(H_2E)_9$ at N-terminus of FTn. HSA-FTn was prepared by genetically incorporation albumin binding domain (ABD) into FTn (FTn-ABD) prior to HSA binding. For the HSA/H_2E-FTn, owing to the FTn composition of 24 subunits, the FTn-ABD and FTn-H_2E were *in situ* self-assembled

into H_2E-ABD-FTn in *E.coli* by taking advantage of a double promotor expression system, followed by mixing and binding with HSA. TEM images showed the structure of FTn and its variants after negative staining (Fig. 4a). Size exclusion chromatography analysis presented the larger molecular sizes of the FTn variants compared to FTn, as indicated by the shorter elution time (Fig. 4b). Importantly, the expected nanostructures with genetic incorporation and/or HSA binding were confirmed, as evidenced by the elution time and the characterization of SDS-PAGE (Fig. 4c). The zeta potential changes of H_2E and HSA/H_2E-FTn from pH7.0 to pH5.0, demonstrating protonation effect of H_2E in mediating FTn-based nanoparticle switching to positive charge in acidic microenvironments (Fig. 4d).

Next, we sought to explore whether the tailored FTn variants improved transport efficacy of endothelial cells. Firstly, we studied the intracellular fate of FTn and its variants, including cell uptake, intracellular trafficking, and exocytosis. Confocal images showed efficient cell uptake of FTn and its variants after incubation with HUVECs (Fig. 5a). Unlike the exclusive distribution of FTn in lysosomes, the various FTn variants partly localized into lysosomes after uptake, and demonstrated the capability of escaping from lysosomes into the cytoplasm. Furthermore, we found that H_2E-FTn, HSA-FTn and HSA/H_2E-FTn co-localized with Golgi, whereas the distribution of FTn was negligible in Golgi (Fig. 5b). By culturing for another 6 hours after uptake, exocytosis of FTn variants was evidently more than that of FTn, as indicated by co-localization with cell membrane (Fig. 5c). Based on the role of Golgi in exocytosis[30,31] and the above results, the potential intracellular fate of FTn and its variants was summarized and is shown in Fig. 5d. We further investigated whether FTn variants could improve translocation of FTn from endothelial cells to tumour cells, as a result of the enhanced exocytosis by Golgi. FITC-labelled FTn and Cy5-labelled FTn/FTn variants were co-incubated with HUVECs seeded onto slides. Subsequently, the slides with HUVECs were then placed into dishes alongside slides seeded with untreated tumour cells. Flow cytometry analysis revealed that transcytosis of FITC-FTn occurred under similar conditions amongst all treatment groups, as evidenced by the consistent FITC signal intensity exhibited by tumour cells (Fig. 5e). In contrast, the Cy5 signal intensity of the tumour cells treated with H_2E-FTn, HSA-FTn and HSA/H_2E-FTn were 2.70-, 3.76- and 4.95-fold higher than that of FTn, respectively, demonstrating the synergistic role of H_2E and HSA in transcytosis. Using the Nano-ISML, we next quantitatively evaluated the vascular permeability of FTn and its variants in HP-tumours or LP-tumours. Confocal images showed the permeability of FTn variants in tumours tissues were stronger than that of FTn, at 30 minutes after administration (**Supplementary Fig. 10**). Quantification analysis of all vessels demonstrated that mean PR of HSA/H_2E-FTn for 3LL, U87 and SKBR3 were increased by 40%, 21% and 37% compared to that of FTn alone within 30 minutes, respectively. In contrast, the mean PR for the vessels of HP-tumours (i.e., HT29, HepG2) showed no clear changes (Fig. 5f). Violin plot analysis demonstrated the improved permeability of FTn variants in LP-tumours (i.e., 3LL, SKBR3, U87) compared to that of FTn (Fig. 5g). However, the changes to nanoparticle vascular permeability resulting from H_2E/HSA incorporation was limited in HP-tumours due to the masking by the VP distribution population in HP-vessels. Quantification analysis revealed that FTn variants converted LP-vessels into the indices that defined MP-vessels in LP-

tumours (Fig. 5h). We also found that HSA/H_2E-FTn showed a greater conversion efficacy than H_2E-FTn and HSA-FTn, implying their synergistic effect on improvement of active trans-endothelial transport.

We next studied whether FTn variants could improve therapeutic outcomes due to enhanced vascular permeability. We first compared *in vivo* behaviours following i.v. administration of FTn and its variants. We found that H_2E and/or HSA incorporation did not significantly affect *in vivo* blood circulation time of FTn (**Supplementary Fig. 11**). *In vivo* tumour accumulation of FTn and its variants was further investigated by imaging and monitoring of both LP-tumours and HP-tumours. To do this, SKBR3 and HT29 were simultaneously inoculated into left shoulder and right shoulder of the same mice, respectively (Fig. 6a**)**. We observed obvious tumour accumulation of FTn and its variants in both LP-tumours and HP-tumours, and greater accumulation was found in HP-tumours compared to that in LP-tumours. Quantification analysis of LP/HP ratio demonstrated that FTn variants resulted in improved LP:HP ratio at 12 hours, compared to that of FTn. The elevated LP:HP ratio at 12 hours was higher than the ratio observed at 1 hour, especially for HSA/H_2E-FTn. These results suggested that the contribution of active trans-endothelial transport was in effect. We next sought to evaluate whether FTn variants could result in *in vivo* improved anti-tumour efficacy. A chemotherapeutic drug, doxorubicin (Dox), was loaded into FTn and its variants (**Supplementary Fig. 12a)**, according to our previously described methodology[32]. The number of Dox molecules loaded into each FTn, H_2E-FTn, HSA-FTn and HSA/H_2E-FTn was determined to be 67.4 ± 5.6, 66.2 ± 3.7, 65.9 ± 4.3 and 59.8 ± 5.9, respectively. Confocal images revealed that the Dox loaded FTn and FTn variants was successfully released after cell uptake and delivered to the nuclei of tumour cells (**Supplementary Fig. 12b**). Subsequently, Dox-loaded FTn (FTn-Dox), Dox-loaded H_2E-FTn (H_2E-FTn-Dox), Dox-loaded HSA-FTn (HSA-FTn-Dox) and Dox-loaded HSA/H_2E-FTn (HSA/H_2E-FTn-Dox) were i.v. injected into the mice xenografted with LP-tumours (i.e., 3LL, SKBR3) and HP-tumours (i.e., HT29) every 3 days. As expected, systemically administered Dox-loaded FTn and its variants significantly delayed tumour growth, regardless of LP-tumours and HP-tumours (Fig. 6b). Compared to H_2E-FTn-Dox and HSA-FTn-Dox, HSA/H_2E-FTn-Dox showed a synergistic therapeutic action in LP-tumours, but this action was not observed in HP-tumours. Survival was also effectively improved for LP-tumours xenografted mice treated with HSA/H_2E-FTn-Dox, compared to H_2E-FTn-Dox and HSA-FTn-Dox. In contrast, HSA/H_2E-FTn-Dox did not significantly delay the survival of HP-tumour-bearing mice compared to FTn-Dox, H_2E-FTn-Dox and HSA-FTn-Dox. These results revealed that improving vascular permeability properties of nanoparticles in LP-tumours positively correlated with therapeutic outcomes, but had no significant effect on HP-tumour penetration, owing to their already existence of highly passive extravasation.

Discussion

Quantitative assessment of tumour vascular permeability is particularly crucial for nanoparticle drug delivery field[33]. Recently, emerging imaging technologies have been applied for quantitative analysis of nanoparticle leakiness in tumour blood vessels, such as three-dimensional (3D) imaging of transparent

tissue[11,34,35] and real-time imaging of dynamic penetration of nanoparticles across vessels with intravital microscopy[36–38]. These advanced technologies achieve a leap from qualification to quantification in the context of determining vascular permeability in tumours, but their bulk analysis exhibits an average result, losing the real features of individual vessels due to highly heterogeneity of vascular microstructures. In this study, we created a ML-based single-vessel quantitative analysis method that was capable of high-throughput assessment of individual blood vessel features. By collecting thousands of vessel sections, this approach enabled correctly quantitative characterization of intratumoural heterogeneity associated with vascular permeability of nanoparticles. Based on the quantitative data, we manually classified permeable tumours into two categories (HP and LP) and permeable vessels into three categories (HP, MP, and LP). This classification of permeability will undoubtedly provide valuable information for developing personalized therapeutic strategies of tumours. For example, our data demonstrated that improving active trans-endothelial transport was not a necessity for HP-tumours, but was essential for efficient delivery in LP-tumours. Additionally, we demonstrated that the approach facilitated understanding heterogeneous permeability mechanisms of blood vessels to accelerate the development of strategies to modulate vascular permeability. The mean VP of different vessel sections were consistent by our observations in this study, but further studies are required to minimize the gap between 2D image information and features obtained from 3D tumour tissues. Future studies are also needed to expand nanoparticle types for elucidating robustness of the approach, and explore the link between animal tumour models and clinical cases, using the single-vessel analysis method. Going forward, we anticipate that the single-vessel analysis method will be particularly useful for the development of highly permeable anti-cancer nanomedicines, and of value in the screening of inducers/inhibitors to modulate vascular permeability. Furthermore, the method may also drive new frontiers in studying the link between spatial distribution features of blood vessels and the progressive development of tumours.

Our results demonstrated that vascular permeability was highly heterogeneous among different tumour types and different blood vessels, as evidenced by mean PR > 5-fold greater in HP-tumours compared to LP-tumours, and single vessels with PR > 100-fold greater in the highest PR vessels compared to the lowest PR vessels. These data revealed that blood vessel features were essential determinants of nanoparticle permeability through the endothelium. However, our studies also support the view that vascular permeability of nanoparticles can be modulated by rational design, more-so in the aim of achieving active trans-endothelial permeability in LP-tumours. Previous studies have demonstrated that increasing the cellular uptake efficiency of endothelial cells is an effective strategy to strengthen active transport across tumour blood vessels[39–41]. However, we found that pinocytosis, a non-specific uptake mechanism, was the predominant capture and uptake mechanism of nanoparticles in LP-tumours. This finding motivated us to seek an alternative trans-endothelial transport mechanism to exploit. Lysosomes play a vital role in determining the fate of the nanoparticles and their intracellular trafficking. Nanoparticles trapped within lysosomes tend to be degraded, which ultimately lowers the payload delivery efficiency of nanoparticles[42]. To improve transcellular trafficking of nanoparticles in endothelial cells, we developed a transcytosis-enhanced strategy by boosting the Golgi-dependent exocytosis

pathway. Protein nanoparticles were designed with integrated lysosome-escaping motifs with HSA-binding motifs, thus aiming to provide a synergistic effect to reduce lysosome degradation by accelerating Golgi exocytosis. The evidence revealed that elevated exocytosis of nanoparticles from endothelial cells would be another ideal design principle for improving trans-endothelial transport, and this was especially important in achieving tumour penetration and drug deliver to LP-tumours. Based on our mechanistic studies, several potential aspects are recommended to boost vascular permeability of nanoparticles in LP-tumours: (i) improve the blood circulation time of nanoparticles to increase the chance of capture and uptake by endothelial cells (i.e. pinocytosis); (ii) actively strengthen nanoparticle-endothelial cell interactions (e.g. non-specific adsorption, receptor-ligand functionalisation) to amplify cell uptake; (iii) accelerate transcytosis of nanoparticles in endothelial cells (e.g. boost exocytosis, minimize nanoparticle degradation); and (iv) selectively improve passive penetration capabilities of tumour blood vessels (e.g. vasodilation). In summary, this study provides an example of a rational approach to finding a solution to the problems faced by the anti-cancer drug delivery field by taking advantage of multidisciplinary technology.

Methods

FTn and its variants

FTn were purified according to our previously reported procedures[43,44]. Briefly, a plasmid encoding human ferritin heavy chain (FTC) gene was transformed into *E. coli* BL21(DE3) competent cells. Subsequently, IPTG was added to induce FTn expression in *E. coli*, and the cells were harvested and resuspended in PBS buffer and lysed by sonication to obtain a transparent lysis solution. The supernatant was then heated at 65°C for 10 minutes to obtain FTn crude solution, followed by purification with Superose 6 increase 10/300 GL column (GE Healthcare) to obtain the pure protein solution.

The H_2E-FTn and ABD-FTn were obtained by genetically incorporating a H_2E repeat (HHEHHEHHEHHEHHEHHEHHEHHE) and ABD (albumin-binding domain, LAEAKVLA NRELDKYGVSDFYKRLINKAKTVEGVEALKLHILAALP) into the FTC gene, respectively. For H_2E-FTn, the inserted H_2E repeats gene were directly ligated into the pET-21a(+) plasmid subjected to ferritin heavy chain gene, with a linker of GGGGS. To incorporate ABD into FTn, FTC and ABD-FTC genes were inserted into the double cis-trans pCDFDuet-1 plasmid, respectively. For ABD/H_2E-FTn, H_2E-FTC and ABD-FTC genes were ligated into double cis-trans pCDFDuet-1 plasmid, which were self-assembled into H_2E-ABD-FTn in the later expression because FTn is composed of 24 subunits. The obtained plasmids were transfected into BL21 *E. coli*. The expression and purification of H_2E-FTn, ABD-FTn and H_2E-ABD-FTn followed the procedures of FTn, as described above. For human serum albumin (HSA) binding, 10 molar equivalents of HSA were reacted with ABD-FTn or ABD/H_2E-FTn at 4°C for overnight, respectively. Subsequently, the resulting mixture was further purified to obtain HSA-FTn and HSA/H_2E-FTn by Superose 6 increase 10/300 GL column, respectively. The concentration of FTn/FTn variants was measured by bicinchoninic acid (BCA) protein assay kit. The morphology of FTn/FTn variants were characterized by

TEM (H7600, Hitachi) following the negative staining using 1% uranyl acetate. The molecular weights and sizes of protein nanocages were determined by SDS-PAGE and size exclusion chromatography. The ζ-potentials of FTn/FTn variants were measured using a Zetasizer Nano ZE (Malvern Instruments).

Labelling and Dox loading of FTn and its variants

For labelling of fluorescence dyes, FTn/FTn variants were reacted with 30 molar equivalents of Cy5-NHS ester or Cy5.5-NHS ester (Lumiprobe) at 4°C for 12 hours in PBS solution (pH 8.0), and then the mixture was purified with a PD-10 desalting column (GE Healthcare). Typically, the conjugated dye number on each nanocage was calculated as 6–8 by determining the concentration of dyes and FTn/FTn variants.

FTn possesses a natural drug entry channel that exists on the shell, which facilitates the direct loading of small molecular drugs into the core. Dox was loaded into FTn and its variants according to our previously reported method[32]. Briefly, 8 mg FTn/FTn variants was reacted with 3 mg Dox at 60°C for 4 hours in 20 mM Tris-HCl buffer (pH 8.0), and then centrifugated at 12,000 rpm for 10 minutes to separate the supernatant, the mixture was then purified with a PD-10 desalting column (GE Healthcare) to remove free Dox. The concentration of protein and Dox complexes were measured by the BCA method and the specific absorbance of Dox at 480 nm, respectively. The number of loaded Dox in each nanocage was calculated based on the protein concentration and Dox concentration.

Tumour models

All animals were handled in accordance with the policies and guidelines of the Animal Ethics Committee of Nankai University. A total of 32 tumour models were successfully constructed by grafting various tumour cells into different mouse species. The established tumour models were classified into three types, including subcutaneous tumours (named with cell lines), orthotopic tumours (i.e., cell line-O) and mouse tumour cells-bearing nude mice (i.e., cell line-N). The subcutaneous tumours were obtained by subcutaneously grafting tumour cells into right shoulder of the mice. Mouse-derived tumour cells were allografted into C57BL/6 or Balb/c mice, and human-derived tumour cells were xenografted into Balb/c-Nude mice. For orthotopic breast cancer model, 4T1 cells were inoculated into the right inguinal fifth mammary fat pad of BALB/c mice. Orthotopic pancreatic tumour model was established by inoculation Panc02 cells into pancreas of C57BL/6 mice. The tumour growth was monitored every day, and tumour volume was calculated as (tumour length) × (tumour width)^2/2. The detailed information on cell lines, cell culture conditions, mouse and tumour models were listed in the **Supplementary Table 3**.

Tumour tissue images

Mice bearing subcutaneous tumour were administrated with Cy5-labeled FTn (30 mg/kg) following tail vein injection when tumours grew to 300–400 mm^3 unless otherwise specified. For orthotopic tumour model, tumour-bearing mice were i.v. injected with Cy5-labeled FTn (30 mg/kg) after implanting tumour cells for 10 days. After 30 minutes administration, the mice were euthanized, and the tumours were harvested to embed into optimal cutting temperature (OCT) compound. Next, the cryosections of tumour tissues were prepared (7 μm thickness) and immunostained with PE-anti-CD31 antibody (BioLegend). To

minimize the effect of spatial distribution on vascular permeability, the resulting cryosections of each tumour type contained the anterior, middle, and posterior segments from at least 4 tumours. Following staining with DAPI, the slices were imaged using confocal microscopy (Zeiss LM710) with Ex/Em 405/461 nm (DAPI for nucleus), Ex/Em 565/578 nm (CD31 for blood vessel) and Ex/Em 633/670 nm (Cy5-labeled FTn), respectively. The acquired parameters of images using confocal microscopy were kept constant in different cryosections of various tumours, especially for acquiring the signal from Cy5-labeled FTn. Given three-dimensional pattern of blood vessels in tumour tissue, at least 1,000 blood vessels were acquired and analysed for each tumour type, to minimize the potential random information from acquired two-dimensional images. For the sequential sections, different tumour tissues (3LL, K180, HT29) were prepared for cryosection. A series of cryosections (7 μm thickness) were obtained. The immunostaining and image acquirement were performed following the above procedures.

For the Zombie model study, the Zombie mice were prepared as described elsewhere with some modifications[11]. Briefly, the mice were anesthetized under a continuous flow of 2.5% isoflurane in oxygen, and then the ribs were opened to expose the heart. A flat-bottomed needle was inserted into the left ventricle and 20 mL of PBS solution containing 10 U/mL heparin sodium was perfused at a constant flow rate of 6 mL/minute using a peristaltic pump. Next, 30 mL of 4% paraformaldehyde solution was perfused at the same flow rate and incubated for 30 minutes to fix the vascular system of the whole mouse. After removing the fixative, the solution containing Cy5-labeled FTn was added and circulated for 30 minutes. The tumours were subsequently harvested from the zombie mice and the images containing blood vessels and FTn penetration were acquired as described above.

Image segmentation and single-vessel analysis.

The source code can be accessed at https://github.com/balabilibili24/Confocal_images_analysis.git. All code is evaluated under Python 3.10.4 (https://www.python.org) unless otherwise stated.

Pre-processing

The raw images acquired from confocal microscopy were firstly pre-processed using Zen 3.1 software. The fluorescence intensity of blood vessels and FTn were adjusted to guarantee the image to be visible clearly and all images from various tumour types were kept constant setting modes. Next, noise and artifacts were removed from the images using Gaussian smoothing processing. Finally, the images were exported for further analysis following adjusting the image size as 1024×1024.

Model training

The classic U-net model has an end-to-end deep learning network, which is typically used as biomedical image segmentation[19]. Using U-net as a basic framework, we developed two models to segment blood vessels and FTn penetration, respectively. The two models are capable of independently segmenting images of two channels (i.e., vessel and FTn penetration) but each vessel and its corresponding penetration were kept interconnected. In a typical model training, approximately 70 representative images

were extracted from 32 tumour types, and the boundary of each vessel or the corresponding FTn penetration in the images was manually annotated. To better quantify the vascular permeability, two kinds of images were excluded to annotate: the images contain the vessel signal but without that of the corresponding FTn, and similarly, the FTn penetration was observed but there were not the corresponding vessels. To reduce bias, three independent researchers annotated the images during this process. The entire annotated images were randomly divided into an 80% training dataset and a 20% validating dataset. The validating set was also divided into two parts, which were used to monitor the segmentation performance of the model by Dice Similarity Coefficient (DSC). Next, the segmentation models are trained using backpropagation, and the hyperparameters of the model were selected by hyperparameter optimization. During the training process, Adam optimisation with a batch size of 4 and the initial learning rate of 0.05 was adopted. Additionally, the maximum epoch number was set to 100. Data augmentation was performed to extend our samples and reduce the overfitting by flip, rotation, and transpose, etc. All processes of segmentation model building and evaluation were implemented using the Pytorch v1.5 deep-learning library on a machine with an NVIDIA RTX3090 GPU.

Feature quantification analysis

All confocal images obtained from various tumours were automatically segmented using the two U-net segmentation models established above. Subsequently, four basic features were extracted, including total FTn coverage area for each vessel (A_{red}), coverage area of each vessel (A_{green}), total Cy5 fluorescence intensity for each vessel (F_{red}) and Cy5 fluorescence intensity in each vessel and its lumen (I_{red}). Based on the four indices, nine important parameters of the images including blood vessels, FTn penetration and the interface between vessel and FTn penetration, were automatically extracted for quantification analysis by the models. Specifically, the extracted features of blood vessels contained vessel density (VD, vessel number per mm^2 tumour tissue), vessel area (VA = A_{green}, coverage area for each vessel), total VA% (the percentage of total VA in total tumour tissue area for each image). The FTn penetration features included penetration area (PA = A_{red}, coverage area of FTn penetration for each vessel), total PA% (the percentage of total PA in total tumour tissue area for each image), FTn penetration amount (FA, penetration amount of FTn for each vessel, FA = PA*F_{red} - VA*I_{red}). For quantification analysis of penetration ability of individual vessel, the interface between vessel and the corresponding FTn penetration was consist of relative penetration area (RA, relative FTn penetration area for each vessel, RA = A_{red} - A_{green}), penetration area ratio (PR, FTn penetration area ratio for each vessel, PR = A_{red} / A_{green}) and vascular permeability (VP, FTn penetration ability for each vessel, VP = FA / (A_{red} *F_{red})). The manual setting parameters and their formulae are listed in **Supplementary Table 1.** Finally, the above nine indices were quantitatively analysed to determine the features of vessel, penetration, and permeability. Details of the extracted indices are shown in **Supplementary Table 2**.

Vascular penetration mechanism

To visualize FTn penetration across tumour blood vessels with TEM, iron oxide nanoparticles were in situ incorporated into the FTn cavity. FTn loaded with iron oxide nanoparticles (FTn-IO) were prepared using

our previously reported method[20]. FTn-IO (equivalent FTn, 250 mg/kg) was administrated via tail vein to 3LL tumour-bearing mice and HT29 tumour-bearing mice, respectively. After 30 minutes, the tumour tissues were harvested, fixed, and processed according to standard procedures for the preparation of biospecimens for TEM. The resulting samples were observed using TEM and the vascular penetration mechanisms were evaluated according to the distribution of observed FTn-IO.

In vivo **near infrared (NIR) tumour imaging**

To understand the in vivo dynamic behaviours of FTn, tumour-bearing Balb/c-Nude mice were intravenously injected with Cy5.5-labeled FTn (30 mg/kg). Subsequently, tumour accumulation profiles were monitored on the front flank tumours of three mice using a Maestro all-optical imaging system at predetermined time points (10, 30, 60 and 180 minutes). NIR fluorescence images of tumours were quantified by measuring NIR fluorescence intensity at the ROI using the Maestro all-optical imaging system and accompanying software.

To compare tumour accumulation of LP-tumours and HP-tumours, Cy5.5-labeled FTn and its variants (equal Cy5.5 for different particles) were administrated into SKBR3- (left shoulder) and HT29 (right shoulder)-bearing mice via tail vein. At specific time points of post-injection (1 and 12 hours), the mice (n = 4/group) were imaged by IVIS Spectrum imaging system (IVIS Lumina II Xenogen, Caliper Life Sciences). The accumulation of FTn in tumours were semi-quantitatively analysed by using a Living Image 2.50 software. All values are expressed as means ± SEM for groups of four animals.

Subcellular location

Human umbilical vein endothelial cells (HUVECs) were seeded on sterile coverslips and cultured overnight. The medium was replaced with fresh medium and Cy5-labeled FTn/FTn variants (20 μg/mL) were added to incubate for 2 hours. For co-localization with lysosomes, the HUVECs were washed with PBS buffer and continued to incubate for additional time points in fresh medium (2, 4, 6 and 8 hours). The cells were stained with LysoTracker Red (100 nM, Thermo Fisher Scientific) and Hoest3342 at 37°C for 15 minutes for co-localization with lysosomes. For co-localization with Golgi, the HUVECs treated with Cy5-labeled FTn/FTn variants were washed with PBS buffer and continued to incubate for 4 hours. The HUVECs were immunostained using anti-GALNT2 antibody (Abcam, ab262868) following the standard procedure. To study exocytosis of HUVECs, the co-localization of FTn/FTn variants with cell membrane was observed. Typically, the HUVECs treated with Cy5-labeled FTn/FTn variants were washed with PBS buffer and continued to culture for additional 6 hours. The cells were stained with DiI (10 μM, Thermo Fisher Scientific) and Hoest3342 at 37°C for 15 minutes. After the above staining, the subcellular location (i.e., lysosome, Golgi and cell membrane) of FTn/FTn variants were observed using Zeiss LM710 confocal microscopy with Ex/Em 405/461nm for nucleus, Ex/Em 565/578nm for lysosome, Golgi or cell membrane and Ex/Em 633/670nm for FTn/FTn variants, respectively.

Transcytosis

To study transcytosis of FTn and FTn variants, the HUVECs were first plated on sterile coverslips in cell culture dishes. FITC-labelled FTn and Cy5-labeled FTn variants (50 μg/mL) were simultaneously added into the HUVECs for 4 hours incubation. The HUVECs were washed with PBS buffer at least three times before subsequent co-culture with coverslips plated with untreated tumour cells. The two cell seeded coverslips were placed in an adjacent configuration within a culture dish containing fresh medium and incubated for an additional 12 hours. Finally, the cells on the different coverslips were harvested and were separately analysed by flow cytometry. The FITC signal of tumours cells were used as control group to determine the assay with similar conditions. The effect of FTn and its variants on transcytosis were determined by the Cy5 signal of tumours cells.

Plasma pharmacokinetics of FTn/FTn variants.

Cy5-labeled FTn/FTn variants was injected into the C57BL/6 mice via tail vein at a dose of approximately 30 mg/kg (equivalent Cy5 for FTn/FTn variants). The blood samples were collected at specific time points (3, 6, 10, 20, 30, 60, 120, 240, 480, 720 and 1,240 minutes), and were then centrifuged at 4,000 rpm for 10 minutes to separate the plasma. The concentrations of the FTn/FTn variants in the plasma were determined by measuring the fluorescence intensity at 640/670 nm.

Cellular uptake of Dox loading FTn/FTn variants

SKBR3 tumour cells were plated on glass bottom dishes (MatTek) at a density of 5×10^3 cell/cm^2 and were cultured for 24 hours prior to use. The cells were incubated with FTn-Dox, H_2E-FTn-Dox, HSA-FTn-Dox or HSA/H_2E-FTn-Dox (at 10 μM Dox concentration) for 4 hours and 12 hours, respectively. After washing with PBS, the cells were fixed with 4% paraformaldehyde for 15 minutes, followed by 1.5 μg/mL DAPI staining at room temperature. The images of cells were acquired with a Zeiss LM710 confocal microscopy.

In vivo **antitumour activity**

For mouse-derived LP-tumour models, female C57BL/6 mice were subcutaneously inoculated with 3LL cells (5×10^5 cells per mouse) into the right flank. After 1 week, the mice were randomly divided into four groups (n = 12 per group) and intravenously administered with PBS, FTn-Dox, H_2E-FTn-Dox, HSA-FTn-Dox and HSA/H_2E-FTn-Dox at 5 mg/kg Dox-equivalent doses every 3 days. To obtain human-derived LP-tumour model, female BALB/c-Nude mice were subcutaneously injected with SKBR3 cells (5×10^6 cells per mouse) in the right flank. After two weeks, the mice were randomly divided into four groups (n = 12 per group). The mice for each group were intravenously administered with PBS, FTn-Dox (5 mg/kg Dox equivalent), H_2E-FTn-Dox (5 mg/kg Dox equivalent), HSA-FTn-Dox (5 mg/kg Dox equivalent) and HSA/H_2E-FTn-Dox (5 mg/kg Dox equivalent) every 3 days. For human-derived HP-tumour model, female BALB/c-Nude mice were subcutaneously injected with HT29 cells (1×10^6 cells per mouse) in the right flank. After 2 weeks, the mice were randomly divided into four groups (n = 12 per group) and subjected to treatments with multiple doses of PBS, FTn-Dox, H_2E-FTn-Dox, HSA-FTn-Dox and HSA/H_2E-FTn-Dox at 5

mg/kg Dox-equivalent doses, following tail vein injection every 3 days. For all the mice, the tumour size and body weight were measured every day. In parallel, survival of animals was monitored daily.

Statistical analysis

Statistical analysis was done using Python and GraphPad Prism 8.0. The statistical difference between two groups and among multiple groups were analysed using Student's t-test and one-way/two-way analysis of variance (ANOVA), respectively. The differences in the survival were analysed using the log-rank test. $P < 0.05$ was considered statistically significant and all the results are expressed as a mean ± standard error mean (SEM).

Declarations

Acknowledgements

We acknowledge the support by the National Natural Science Foundation of China (91959129, 82072054, 31870999), Tianjin Synthetic Biotechnology Innovation Capacity Improvement Project (TSBICIP-KJGG-014-03), Nankai University Hundred Young Academic Leaders Program.

Author contributions

M.Z., J.Z. and X.H. conceived the idea, collected data, conducted data analysis, and performed all experiments. Z.L. assisted the development of U-net model. M.Z. and X.H conducted data information from U-net. Q.L., Z.G., Z.Z., T.Q. and R.Z. performed cryosections and immunostaining. A.C.M. provided guidance and edited the manuscript. D.K., and J.T. helped to guide part of experiments. X.Y. and X.H. designed and supervised all studies and wrote the manuscript.

Competing interests

The authors declare no competing interests.

Additional information

Supplementary Information is available for this paper at http://doi.org/.

Correspondence and requests for materials should be addressed to X.H.

References

1. Shi, J., Kantoff, P. W., Wooster, R. & Farokhzad, O. C. Cancer nanomedicine: progress, challenges and opportunities. Nat Rev Cancer **17**, 20–37, doi:10.1038/nrc.2016.108 (2017).
2. Minchinton, A. I. & Tannock, I. F. Drug penetration in solid tumours. Nat Rev Cancer **6**, 583–592, doi:10.1038/nrc1893 (2006).
3. Jain, R. K. & Stylianopoulos, T. Delivering nanomedicine to solid tumors. Nat Rev Clin Oncol **7**, 653–664, doi:10.1038/nrclinonc.2010.139 (2010).
4. Blanco, E., Shen, H. & Ferrari, M. Principles of nanoparticle design for overcoming biological barriers to drug delivery. Nat Biotechnol **33**, 941–951, doi:10.1038/nbt.3330 (2015).
5. Huang, X. *et al.* Hypoxia-tropic Protein Nanocages for Modulation of Tumor- and Chemotherapy-Associated Hypoxia. ACS Nano **13**, 236–247, doi:10.1021/acsnano.8b05399 (2019).
6. Dvorak, A. M. *et al.* The vesiculo-vacuolar organelle (VVO): a distinct endothelial cell structure that provides a transcellular pathway for macromolecular extravasation. J Leukoc Biol **59**, 100–115 (1996).
7. Dvorak, A. M. & Feng, D. The vesiculo-vacuolar organelle (VVO). A new endothelial cell permeability organelle. J Histochem Cytochem **49**, 419–432, doi:10.1177/002215540104900401 (2001).
8. Claesson-Welsh, L. Vascular permeability–the essentials. Ups J Med Sci **120**, 135–143, doi:10.3109/03009734.2015.1064501 (2015).
9. Matsumura, Y. & Maeda, H. A new concept for macromolecular therapeutics in cancer chemotherapy: mechanism of tumoritropic accumulation of proteins and the antitumor agent smancs. Cancer Res **46**, 6387–6392 (1986).
10. de Lazaro, I. & Mooney, D. J. Obstacles and opportunities in a forward vision for cancer nanomedicine. Nat Mater **20**, 1469–1479, doi:10.1038/s41563-021-01047-7 (2021).
11. Sindhwani, S. *et al.* The entry of nanoparticles into solid tumours. Nat Mater **19**, 566–575, doi:10.1038/s41563-019-0566-2 (2020).
12. Butler, K. T., Davies, D. W., Cartwright, H., Isayev, O. & Walsh, A. Machine learning for molecular and materials science. Nature **559**, 547–555, doi:10.1038/s41586-018-0337-2 (2018).
13. Greener, J. G., Kandathil, S. M., Moffat, L. & Jones, D. T. A guide to machine learning for biologists. Nat Rev Mol Cell Biol **23**, 40–55, doi:10.1038/s41580-021-00407-0 (2022).
14. Moen, E. *et al.* Deep learning for cellular image analysis. Nat Methods **16**, 1233–1246, doi:10.1038/s41592-019-0403-1 (2019).
15. Greenwald, N. F. *et al.* Whole-cell segmentation of tissue images with human-level performance using large-scale data annotation and deep learning. Nat Biotechnol **40**, 555–565, doi:10.1038/s41587-021-01094-0 (2022).
16. Wei, Y. *et al.* Prediction and Design of Nanozymes Using Explainable Machine Learning. *Adv Mater*, e2201736, doi:10.1002/adma.202201736 (2022).
17. Lin, X. *et al.* Chimeric ferritin nanocages for multiple function loading and multimodal imaging. Nano Lett **11**, 814–819, doi:10.1021/nl104141g (2011).

18. Fan, K. *et al.* Magnetoferritin nanoparticles for targeting and visualizing tumour tissues. Nat Nanotechnol **7**, 459–464, doi:10.1038/nnano.2012.90 (2012).
19. Ronneberger, O., Fischer, P. & Brox, T. U-Net: Convolutional Networks for Biomedical Image Segmentation. Lect Notes Comput Sc **9351**, 234–241, doi:10.1007/978-3-319-24574-4_28 (2015).
20. Zhang, Y. *et al.* Biomimetic Design of Mitochondria-Targeted Hybrid Nanozymes as Superoxide Scavengers. Adv Mater **33**, e2006570, doi:10.1002/adma.202006570 (2021).
21. Nagy, J. A., Chang, S. H., Shih, S. C., Dvorak, A. M. & Dvorak, H. F. Heterogeneity of the tumor vasculature. Semin Thromb Hemost **36**, 321–331, doi:10.1055/s-0030-1253454 (2010).
22. Feng, D., Nagy, J. A., Dvorak, A. M. & Dvorak, H. F. Different pathways of macromolecule extravasation from hyperpermeable tumor vessels. Microvasc Res **59**, 24–37, doi:10.1006/mvre.1999.2207 (2000).
23. Kaksonen, M. & Roux, A. Mechanisms of clathrin-mediated endocytosis. Nat Rev Mol Cell Biol **19**, 313–326, doi:10.1038/nrm.2017.132 (2018).
24. Bonam, S. R., Wang, F. & Muller, S. Lysosomes as a therapeutic target. Nat Rev Drug Discov **18**, 923–948, doi:10.1038/s41573-019-0036-1 (2019).
25. Rennick, J. J., Johnston, A. P. R. & Parton, R. G. Key principles and methods for studying the endocytosis of biological and nanoparticle therapeutics. Nat Nanotechnol **16**, 266–276, doi:10.1038/s41565-021-00858-8 (2021).
26. Tai, W., Li, J., Corey, E. & Gao, X. A ribonucleoprotein octamer for targeted siRNA delivery. Nat Biomed Eng **2**, 326–337, doi:10.1038/s41551-018-0214-1 (2018).
27. Bern, M. *et al.* An engineered human albumin enhances half-life and transmucosal delivery when fused to protein-based biologics. Sci Transl Med **12**, doi:10.1126/scitranslmed.abb0580 (2020).
28. Yokota, S. & Fahimi, H. D. Immunocytochemical localization of albumin in the secretory apparatus of rat liver parenchymal cells. Proc Natl Acad Sci U S A **78**, 4970–4974, doi:10.1073/pnas.78.8.4970 (1981).
29. Shroyer, K. R. & Nakane, P. K. Immunohistochemical localization of albumin and in situ hybridization of albumin mRNA. Cell Biochem Funct **5**, 195–210, doi:10.1002/cbf.290050307 (1987).
30. Pelletier, L., Jokitalo, E. & Warren, G. The effect of Golgi depletion on exocytic transport. Nat Cell Biol **2**, 840–846, doi:10.1038/35041089 (2000).
31. De Matteis, M. A. & Luini, A. Exiting the Golgi complex. Nat Rev Mol Cell Biol **9**, 273–284, doi:10.1038/nrm2378 (2008).
32. Jiang, B. *et al.* A natural drug entry channel in the ferritin nanocage. *Nano Today* **35**, doi:ARTN 10094810.1016/j.nantod.2020.100948 (2020).
33. Chauhan, V. P. *et al.* Normalization of tumour blood vessels improves the delivery of nanomedicines in a size-dependent manner. Nat Nanotechnol **7**, 383–388, doi:10.1038/Nnano.2012.45 (2012).
34. Dai, Q. *et al.* Quantifying the Ligand-Coated Nanoparticle Delivery to Cancer Cells in Solid Tumors. ACS Nano **12**, 8423–8435, doi:10.1021/acsnano.8b03900 (2018).

35. Kingston, B. R. *et al.* Specific Endothelial Cells Govern Nanoparticle Entry into Solid Tumors. ACS Nano **15**, 14080–14094, doi:10.1021/acsnano.1c04510 (2021).
36. Matsumoto, Y. *et al.* Vascular bursts enhance permeability of tumour blood vessels and improve nanoparticle delivery. Nat Nanotechnol **11**, 533–538, doi:10.1038/nnano.2015.342 (2016).
37. Zhou, Q. *et al.* Enzyme-activatable polymer-drug conjugate augments tumour penetration and treatment efficacy. Nat Nanotechnol **14**, 799–809, doi:10.1038/s41565-019-0485-z (2019).
38. Chen, S. *et al.* Enhanced tumour penetration and prolonged circulation in blood of polyzwitterion-drug conjugates with cell-membrane affinity. Nat Biomed Eng **5**, 1019–1037, doi:10.1038/s41551-021-00701-4 (2021).
39. Abumrad, N. A. *et al.* Endothelial Cell Receptors in Tissue Lipid Uptake and Metabolism. Circ Res **128**, 433–450, doi:10.1161/CIRCRESAHA.120.318003 (2021).
40. Dewhirst, M. W. & Secomb, T. W. Transport of drugs from blood vessels to tumour tissue. Nat Rev Cancer **17**, 738–750, doi:10.1038/nrc.2017.93 (2017).
41. Chen, S. Q. *et al.* Enhanced tumour penetration and prolonged circulation in blood of polyzwitterion-drug conjugates with cell-membrane affinity. Nat Biomed Eng **5**, 1019-+, doi:10.1038/s41551-021-00701-4 (2021).
42. Smith, S. A., Selby, L. I., Johnston, A. P. R. & Such, G. K. The Endosomal Escape of Nanoparticles: Toward More Efficient Cellular Delivery. Bioconjug Chem **30**, 263–272, doi:10.1021/acs.bioconjchem.8b00732 (2019).
43. Huang, X. *et al.* Protein nanocages that penetrate airway mucus and tumor tissue. Proc Natl Acad Sci U S A **114**, E6595-E6602, doi:10.1073/pnas.1705407114 (2017).
44. Liu, Q. *et al.* Modular Assembly of Tumor-Penetrating and Oligomeric Nanozyme Based on Intrinsically Self-Assembling Protein Nanocages. Adv Mater **33**, e2103128, doi:10.1002/adma.202103128 (2021).

Figures

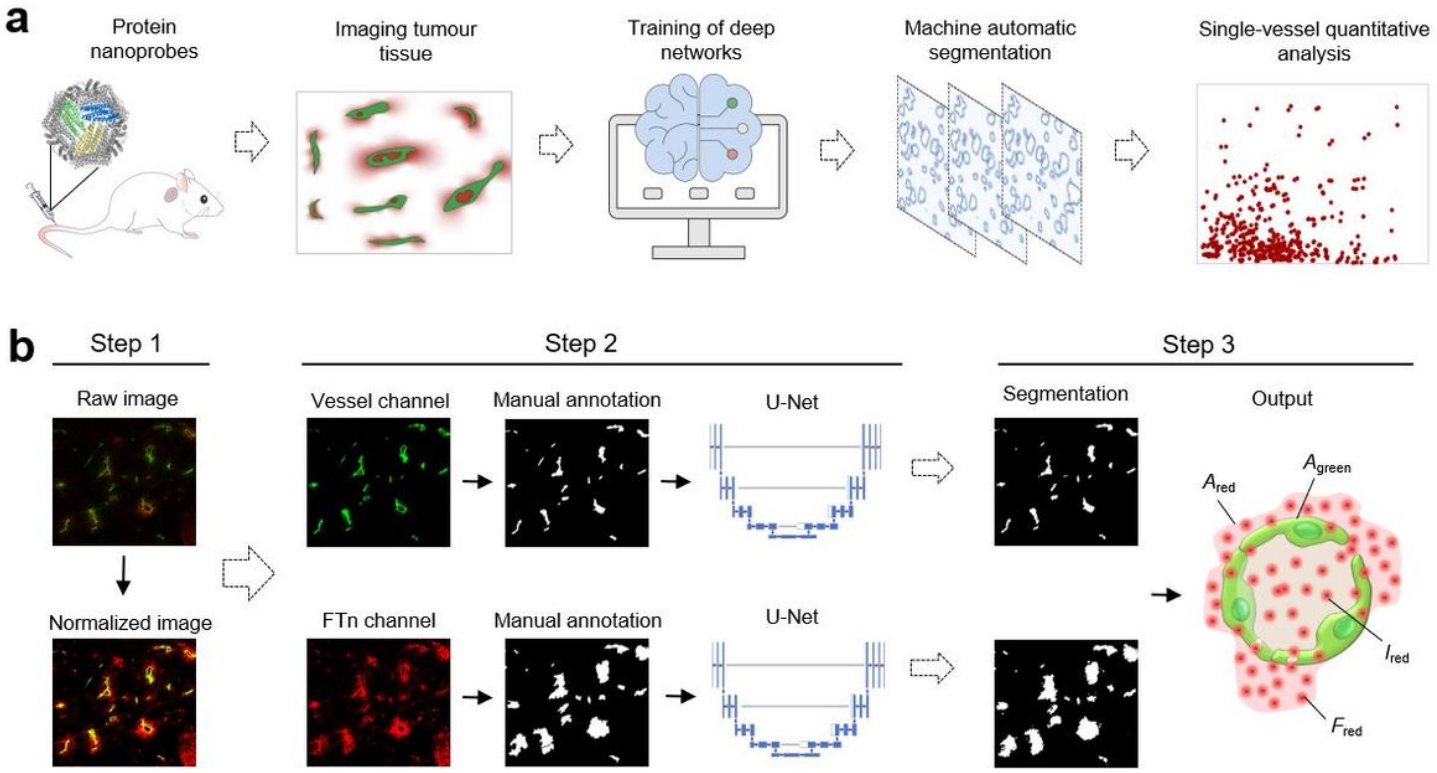

Figure 1

Machine learning-based single-vessel analysis method. a, This approach includes multiple steps. Firstly, the images containing spatial distribution of vessel and protein nanoprobes were acquired following systemic administration via the tail vein of tumour-bearing mice. Next, manually annotated images were trained using a deep neural network. The collected images from various tumour tissues were automatically segmented using the trained models. Finally, the features of input images were automatically segmented and quantitatively analysed. **b**, A detailed workflow for ML-based automatic image segmentation and quantification analysis. During step 1, the images of tumour tissues were pre-processed. During step 2, two-channel images including vessel channel and nanoprobe channel were separated and their boundaries were manually annotated, respectively. The ML-based models were established by training of manually annotated images using U-net convolutional neural network. During step 3, using the established image segmentation models, a large amount of collected images were input for machine automatic segmentation. The quantification information was also automatically output in terms of manually setting indices. A_{red}, total FTn coverage area for each vessel; A_{green}, coverage area of each vessel; F_{red}, total Cy5 fluorescence intensity for each vessel; I_{red}, Cy5 fluorescence intensity in each vessel and its lumen.

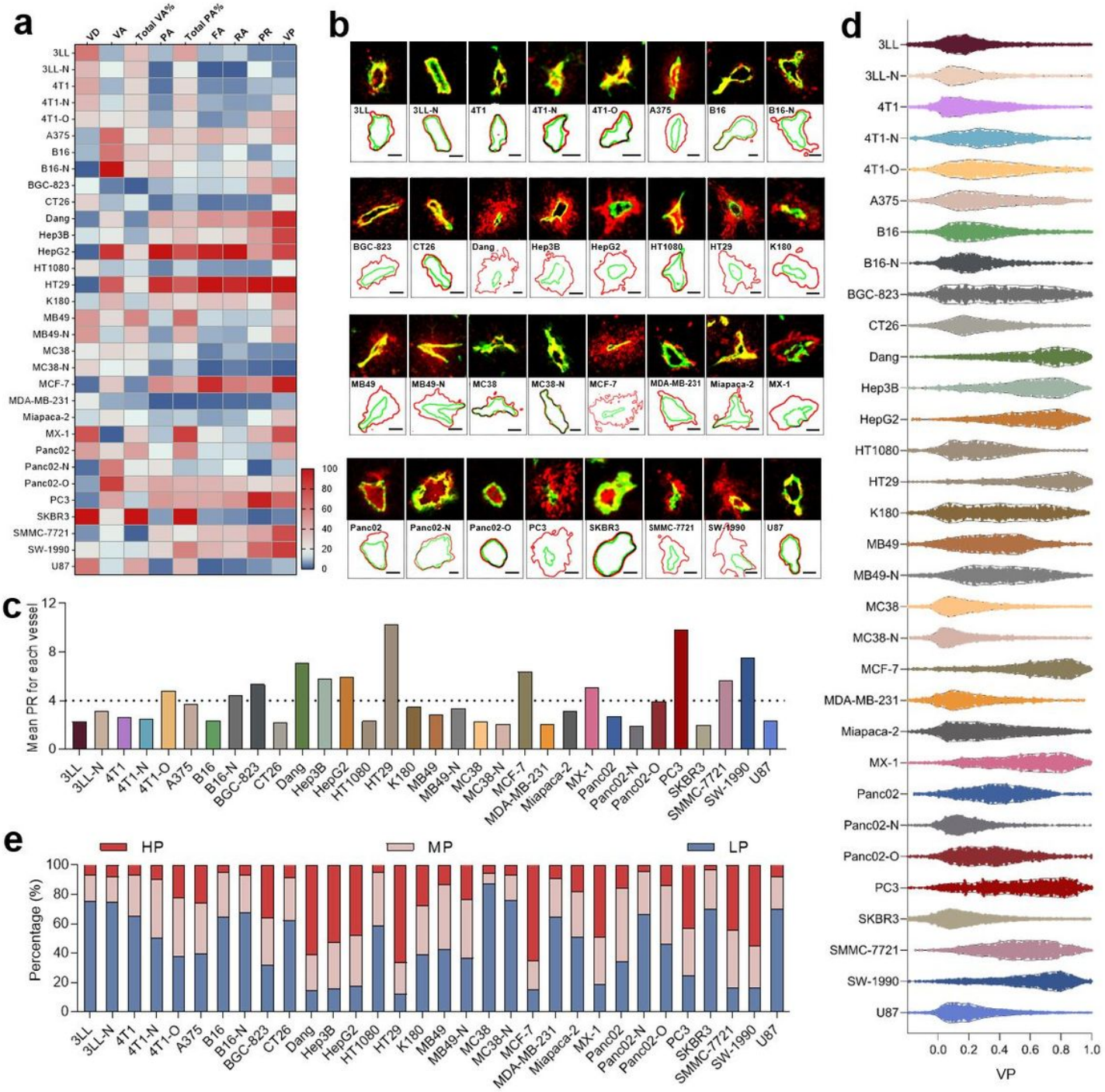

Figure 2

Quantification analysis of heterogeneous vascular permeability using the Nano-ISML method. a, Heatmap showing the penetration patterns of blood vessels for 32 tumour models with rows corresponding to tumour models and columns corresponding to vessels and FTn penetration. The colour scale shows the normalized values by normalizing the maximum value for each parameter as 100. **b**, The representative vessels of FTn away from vessels for 32 tumour models. For each tumour model, the mean PR of each single vessel was extracted. Upper, confocal image for vessel (green) and FTn penetration (red); lower, the output image from ML-based model. Scale bar = 20 μm. **c**, Mean PR for each

vessel in various tumour models. Tumours were manually divided into HP-tumour and LP-tumour based on cut-off value of PR as 4, as indicated by the dash line. **d**, Violin plot analysis of the heterogeneous distribution of VP for each vessel in 32 tumour models. Each dot represents the VP value of single vessel, and at least 1000 vessels were analysed for each tumour model. **e**, All vessels for each tumour model were manually divided into three permeable types according to their VP values, including HP-vessel (> 0.6, ≤ 1), MP-vessel (≥0.3, ≤ 0.6) and LP-vessel (< 0.3). The percentage of three permeable types in all vessels were calculated based on the setting cut-off values.

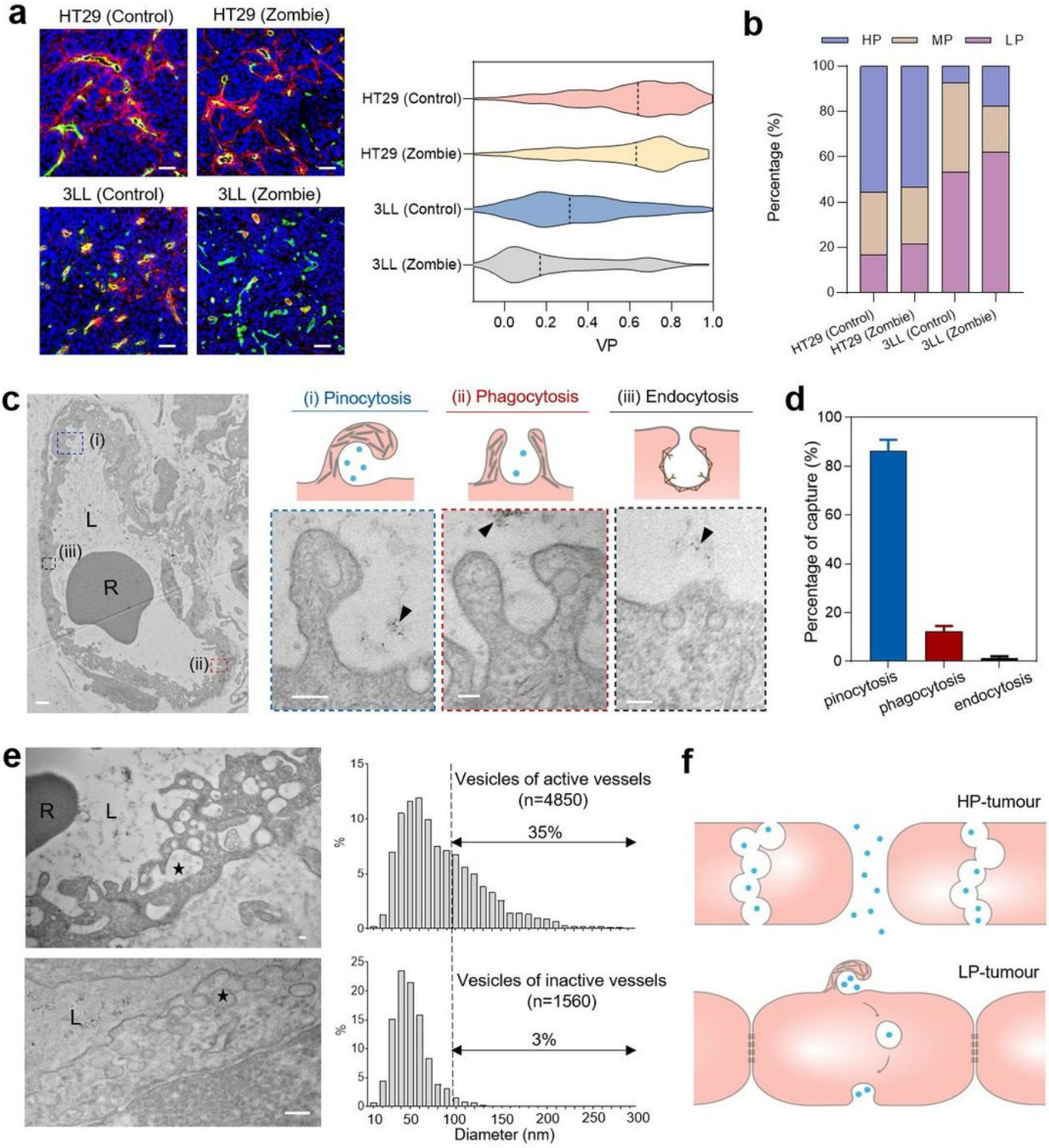

Figure 3

Heterogeneity of vascular permeable mechanism. a, Zombie model with HT29 and 3LL demonstrates active or passive pathway for FTn penetration. The model was developed by fixing the mouse and then the mice were i.v. injected with Cy5-labeled FTn. Compared to control mice, the active pathway of the Zombie mice was blocked, allowing for determining the contribution of two pathways. Left, representative confocal images for vascular penetration in control and Zombie mice, scale bar = 50 μm; right, Violin plot analysis of VP distribution using the Nano-ISML approach. **b**, Quantification analysis of the percentage of HP-, MP- and LP-vessels in control mice and Zombie mice from a. **c**, TEM images of active capture mechanisms of endothelial cells. Representative images for entire vessel (left, scale bar = 1 μm) and enlarged images (right, scale bar = 100 nm) of three typical capture mechanisms (i.e., pinocytosis, phagocytosis and endocytosis). L and R represent lumen of endothelial cell and red blood cell, respectively. Black triangles indicate the FTn-IO in the enlarged images. **d**, Quantification analysis of the contribution of three capture mechanisms for active pathway by counting FTn-IO numbers observed in 73 tumour blood vessels. **e**, The typical features of formed vesicles (black star) in active vessels and inactive vessels. Representative TEM images of formed large vesicles for active vessel (top left) and small vesicles for inactive vessel (bottom left), scale bar = 100 nm; Quantification analysis of the distribution of vesicle diameters in active vessels (top right, n=4850) and inactive vessels (bottom right, n=1560). **f**, Diagram illustrating the dominant vascular penetration mechanism in HP-tumours and LP-tumours. HP-tumours are primarily dependent on the passive extravasation mechanism *via* inter-endothelial gap and VVO pathways, whereas active trans-endothelial transport mechanism following pinocytosis is the dominant manner for LP-tumours.

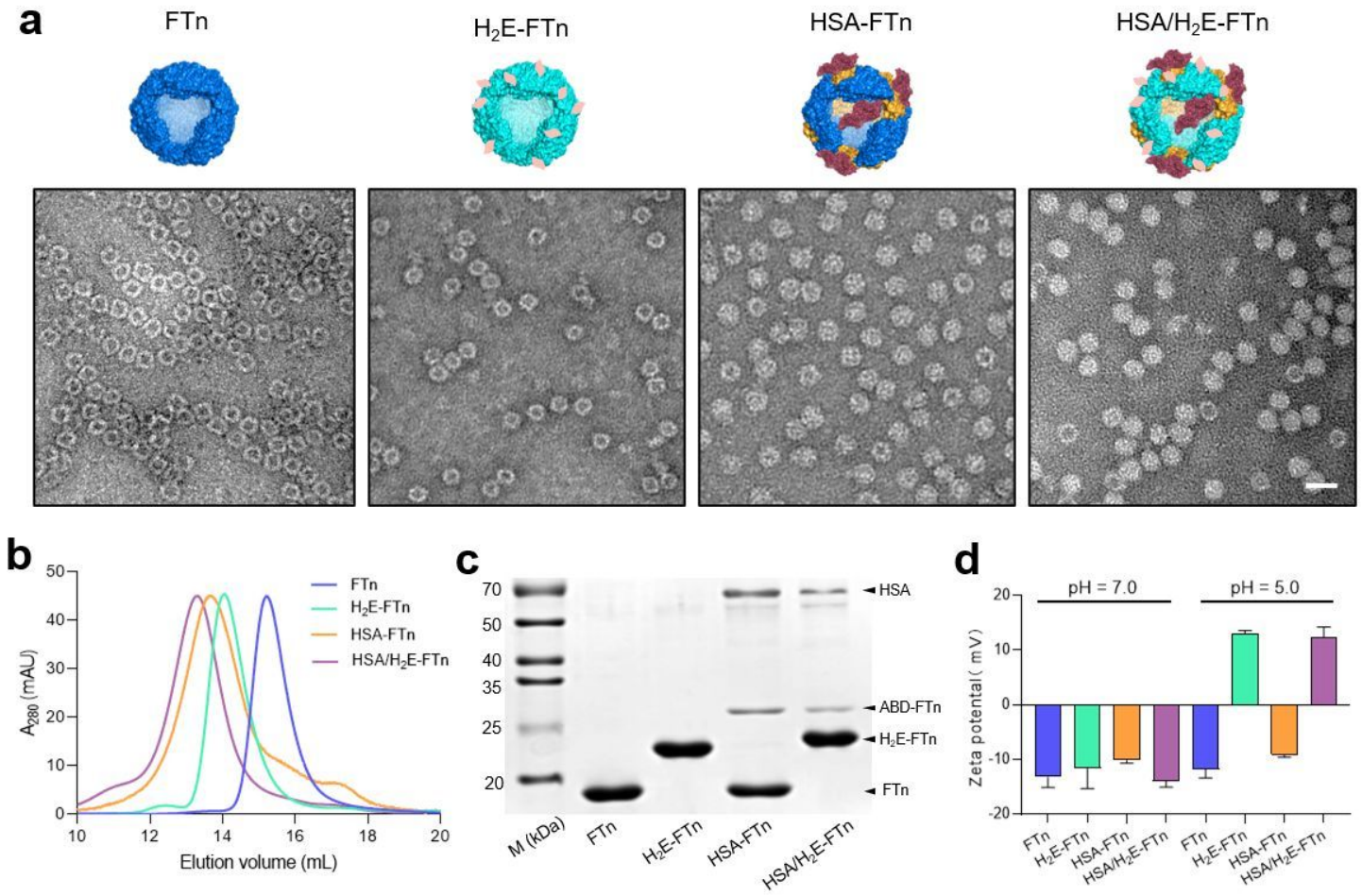

Figure 4

Characterization of FTn and FTn variants. a, Diagrammatic representations and corresponding TEM images of FTn and its variants. The $(H_2E)_9$ fragments (pink) were directly incorporated into FTn subunits. Prior to HSA binding (red), an ABD fragment (orange) was genetically incorporated into FTn subunit, followed by self-assembly with FTn subunit. For HSA/H_2E-FTn, FTn subunits containing H_2E or ABD fragment was self-assembled into single particle, which was further bound with HSA. Scale bar = 20 nm. **b**, Size exclusion chromatography analysis of the sizes of FTn and its variants in protein purification equipment. **c**, SDS-PAGE gel electrophoresis analysis of the resulting FTn and its variants. **d**, Zeta potential of FTn and its variants at pH 7.0 and pH 5.0.

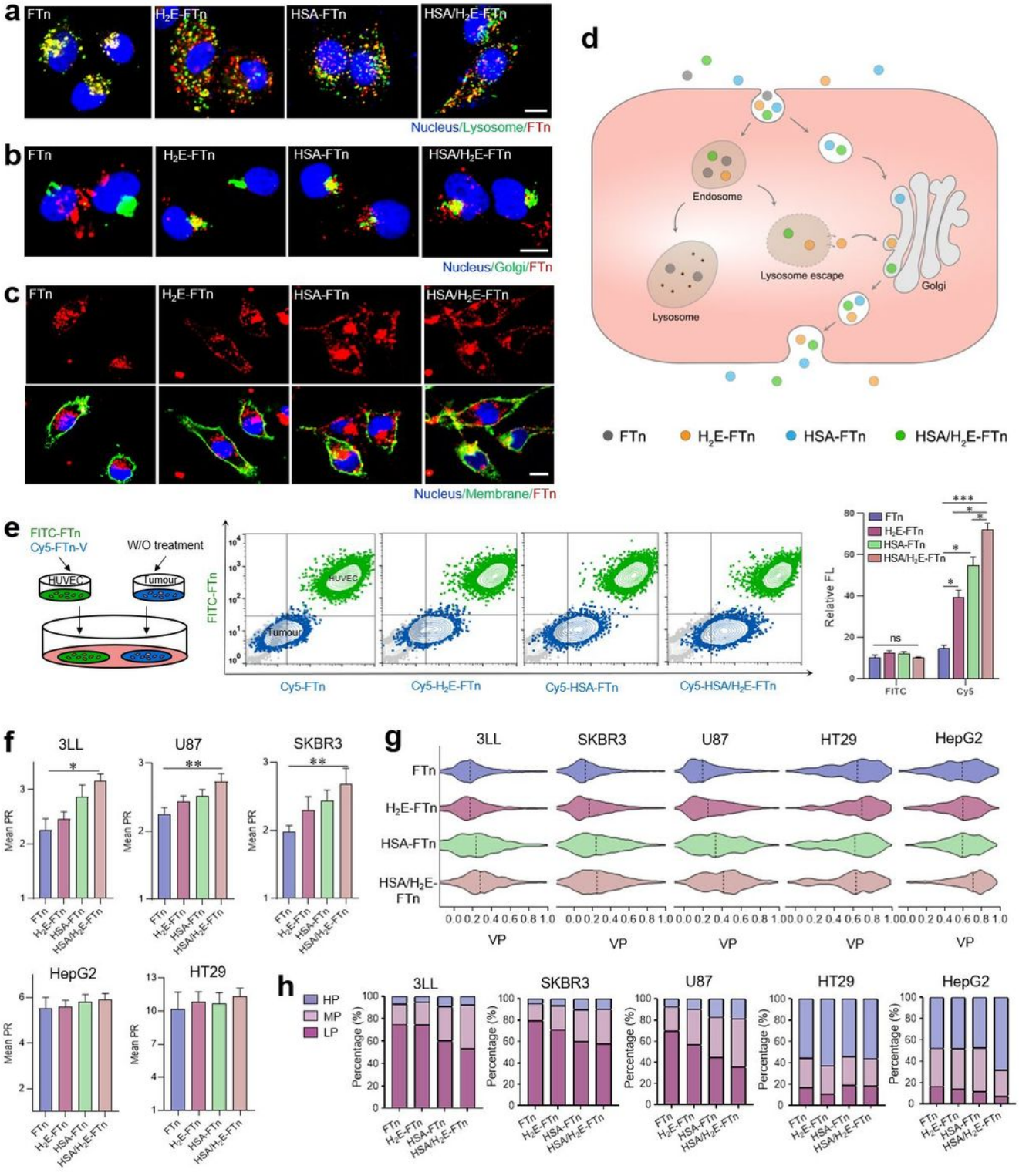

Figure 5

Enhancement of active trans-endothelial transport. Confocal images of HUVECs demonstrating co-localization (yellow) of FTn/FTn variants (red) with lysosomes (**a**, green), Golgi (**b**, green) and membrane (**c**, green). Scale bar = 5 μm. **d**, Schematic illustration shows a transcytosis-enhanced strategy of endothelial cells by boosting Golgi-dependent exocytosis pathway. After uptake, FTn are easily trapped into lysosomes and are further degraded. For H_2E incorporation, the particles are capable of escaping

from lysosomes, followed by exocytosis *via* Golgi-dependent pathway. The HSA binding particles directly traffic into Golgi for exocytosis. The exocytosis of HSA/H_2E-FTn is dependent on the two manners above. **e**, Flow cytometry analysis of transcytosis mechanism by co-incubation of HUVECs and tumour cells. The HUVECs seeded onto coverslip slides (green) were pre-treated with FITC-labelled FTn and Cy5-labeled FTn variants (FTn-V) and the untreated tumour cells were seeded onto another coverslip slide (blue). The tumour cells with fluorescence signal (FITC and Cy5) were collected for quantification analysis using flow cytometry. *$p < 0.05$. ***$p < 0.001$. **f**, Mean PR of blood vessels in various tumours after treatment with FTn and its variants for 30 minutes. *$p < 0.05$. **$p < 0.01$. **g**, Violin plot analysis of the distribution of VP for each vessel in different tumour models using the Nano-ISML approach following administration of FTn and its variants for 30 minutes. **h**, Quantification analysis of the percentage of HP-, MP- and LP-vessels in different tumour-bearing mice treated with FTn and its variants, obtained from g.

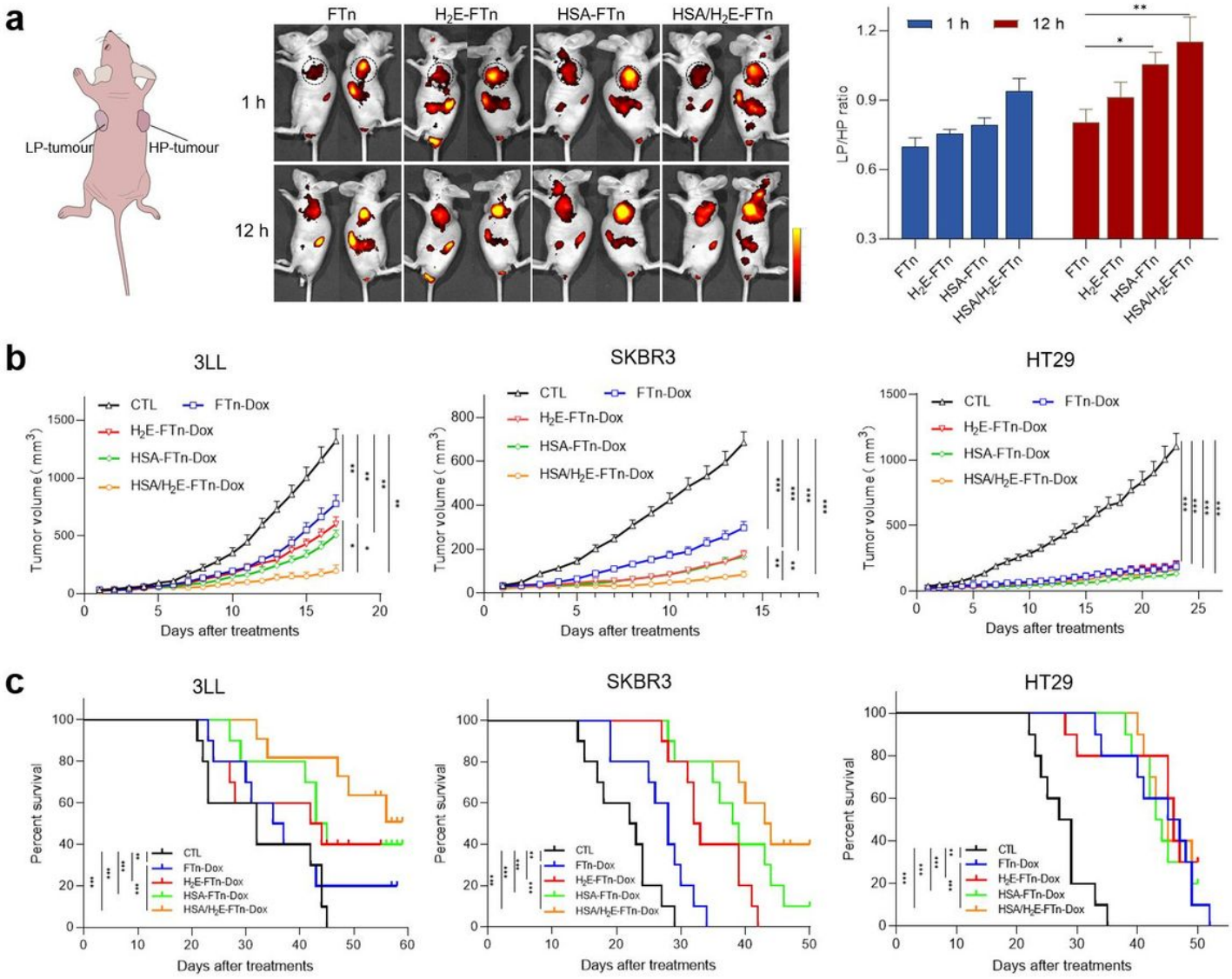

Figure 6

***In vivo* anti-cancer ability of different FTn formulations. a,** *In vivo* fluorescent imaging and quantification analysis of FTn and its variants distribution in mice bearing both LP-tumour (left) and HP-tumour (right) following i.v. injection for 1 hour and 12 hours. The quantification analysis was performed by determining the signal intensity of LP-tumour/HP-tumour ratio in the same mouse (n = 4 per group). Tumours are indicated with black circles. *p < 0.05. **p < 0.01. **b**, Tumour growth curves of different groups of various tumour-bearing mice after administration of the indicated treatments (n = 12 per group). *p < 0.05, **p < 0.01, ***p < 0.001. **c**, Kaplan–Meier survival curve of the different tumour-bearing mice following different treatments (n = 12 per group). **p < 0.01, ***p < 0.001.

Supplementary Files

This is a list of supplementary files associated with this preprint. Click to download.

- SupplementaryMaterials.docx